Linking wall shear stress and vorticity topologies: Toward a unified theory of cardiovascular flow disturbances

# Linking Wall Shear Stress and Vorticity Topologies: Towards a Unified Theory of Cardiovascular Flow Disturbances

Valentina Mazzi[1], Diego Gallo[1], Karol Calò[1], David A. Steinman[2], Umberto Morbiducci[1*]

[1] *PoliTo$^{BIO}$Med Lab, Department of Mechanical and Aerospace Engineering, Politecnico di Torino, Turin, Italy;*

[2] *Biomedical Simulation Laboratory, Department of Mechanical & Industrial Engineering, University of Toronto, Toronto, ON Canada*

The editorial version of this article is available at
https://pubs.aip.org/aip/pof/article-abstract/36/6/061905/3297912/Linking-wall-shear-stress-and-vorticity-topologies?redirectedFrom=fulltext

*** Corresponding author:**

Umberto Morbiducci, PhD

PoliTo$_{BIO}$Med Lab

Department of Mechanical and Aerospace Engineering

Politecnico di Torino

Corso Duca degli Abruzzi, 24

10129 Turin, Italy

ORCID: 0000-0002-9854-1619

E-mail: umberto.morbiducci@polito.it

## Abstract

Broadening current knowledge about the complex relationship at the blood-vessel wall interface is a main challenge in hemodynamics research. Moving from the consideration that wall shear stress (WSS) provides a signature for the near-wall velocity dynamics and vorticity is considered the skeleton of fluid motion, here we present a unified theory demonstrating the existing link between surface vorticity (SV) and WSS topological skeletons, the latter recently emerged as a predictor of vascular disease. In detail, the analysis focused on WSS and SV fixed points, i.e. points where the respective fields vanish, as they play a major role in shaping the main vector field features. The theoretical analysis proves that: (i) all SV fixed points on the luminal surface must necessarily be WSS fixed points, although with differences in nature and stability; (ii) a WSS fixed point is not necessarily a SV fixed point. In the former case, WSS fixed points are the consequence of flow patterns where only shear contributes to vorticity; in the latter case, WSS fixed points are the consequence of flow impingement to/emanation from the vessel wall. Moreover, fluid structures interacting with the wall characterized by zero or non-zero rotational momentum generate WSS fixed points of different nature/stability. High-fidelity CFD simulations in intracranial aneurysm models confirmed the applicability of the theoretical considerations. In conclusion, the presented unified theory unambiguously explains the mechanistic link between near-wall flow disturbances and the underlying intravascular flow features expressed in terms of vorticity, ultimately facilitating a clearer interpretation of the role of local hemodynamics in vascular pathophysiology.

## 1. Introduction

The pathogenesis of vascular diseases is modulated by a complex interplay of risk factors of different natures. This interplay among systemic, biological, and hemodynamic factors leading to vascular

pathology has been suggested acting as a triad, in analogy to Virchow's triad of thrombosis [1]. In particular, the pivotal role played by local hemodynamics in vascular pathophysiology has long been recognized [2–4], and it has been collecting more and more confirmation from studies on animal models and humans (not exhaustively, see [5–8]).

The emerged role of local hemodynamics has stimulated the need for an in-depth understanding of the existing link between blood flow disturbances and clinical observations, aiming at identifying the mechanisms of action of fluid forces on the endothelial machinery. In this regard, particular attention has been paid to the investigation of the hemodynamic environment in the near-wall region, which regulates (i) the local biotransport processes at the interface between streaming blood and arterial wall [4], and (ii) the mechanical stimuli to the endothelium [9]. The actions exerted by fluid friction forces on the vessel luminal surface have been historically interpreted in terms of wall shear stress (WSS), a biomechanical quantity modulating the endothelial function through the activation of the mechanosensing and mechanotransduction machinery regulating endothelial cell gene expression and response via specialized mechanisms and signaling pathways [10]. In the attempt to unveil the mechanisms behind vascular pathophysiology involving local hemodynamics, a plethora of WSS-based quantities has been proposed over the years as potential markers, predictors, and/or localizing factors of vascular wall dysfunction. However, only moderate (and sometimes contradictory) associations between vascular disease and the proposed WSS-based quantities have emerged to date [11–13]. Recently, the analysis of the WSS in terms of its topological skeleton has attracted a strong research interest [9,14–21] and has revealed the ability of WSS topological features to e.g. (i) identify local wall degeneration in the ascending thoracic aorta [22], (ii) predict long-term restenosis risk after carotid endarterectomy [23], (iii) predict plaque progression at an early stage in coronary arteries [8,24], (iv) provide a template of blood-wall mass transfer in vascular territories [9,25,26], (v) predict future myocardial infarction in coronary arteries [6].

Based on dynamical system theory, the WSS topological skeleton is composed of fixed points, focal points where WSS locally vanishes, and unstable/stable manifolds, i.e. regions linking fixed points where the WSS is expected to exert a contraction/expansion action on the endothelial cells [15]. Stricto sensu, an analysis of the WSS topological skeleton is deemed biologically relevant because of its capability to reflect cardiovascular flow features like flow separation, stagnation, and impingement points that are known to be promoting factors for vascular disease [14,15].

An aspect that has been scarcely explored in the study of cardiovascular flows, however, is related to the clear identification of those *intravascular* fluid structures that may leave their peculiar footprints on the vessel wall, thus unambiguously shaping the WSS topological features. To unveil the intravascular fluid structures that condition WSS topology interacting with the luminal surface, fluid mechanics theory as well as *in vivo*, *in vitro,* and *in silico* observation of cardiovascular flows point to vorticity as the *'sinews and muscles of fluid motions'* [27]. In this regard, vorticity transport and vorticity-derived quantities such as helicity have been suggested to play roles of remarkable physiological significance in terms of: (i) energetics, with beneficial impact e.g. in the hemodynamics of heart chambers [28,29], in redirecting blood flow in the total cavopulmonary connection [30], and in minimizing transition to turbulence in aorta [31,32]; (ii) atheroprotective action exerted on the endothelium [33–35], in general contributing to properly balance blood transport and stresses on the surrounding tissues [36]. In addition to these beneficial impacts, vorticity and derived quantities such as enstrophy signatures have been suggested to play a detrimental role in cardiovascular flows, e.g. in coronary arteries [37–39], in intracranial aneurysms [17,40–44], and in abdominal aortic aneurysms [45–47].

Driven by the need to unveil how intravascular fluid structures shape WSS on the luminal surface of the vessel, in this study a unified theory is proposed to link vorticity and WSS topologies. In detail, since in wall-bounded (incompressible) flows the no-slip walls are a unique source of vorticity [48] and a vortex filament cannot end in a fluid (it must extend to the boundaries of a fluid or

form a closed path, according to the Helmholtz's second theorem), the link between the topological skeletons of WSS and surface vorticity (SV), i.e., the vorticity on the luminal surface of the vessel, is analyzed.

Extending previous works proposing a methodology for studying the structure of turbulence in the boundary layer at the no-slip wall [49,50], here we link WSS and SV fields topologies in cardiovascular flows. In particular, here we distinguish the cases when the SV component locally normal to the vessel wall is null from cases when it is not. The rationale of our study is that clarifying the links between WSS and SV fixed points and manifolds can allow for unambiguous deciphering of the nature of the local interactions between intravascular hemodynamics and the vessel wall, thus providing a clear interpretation of the phenomena at the lumen-endothelium interface, and ultimately contributing to a less elusive definition of those "flow disturbances" associated with aggravating biological events. Here, high fidelity CFD simulations of the hemodynamics in intracranial aneurysms, typically characterized by complex and unstable intra-aneurysmal flow [51], are used as explanatory examples to (i) assess the veracity of the demonstrated theoretical links between WSS and SV topology, and (ii) unambiguously identify those intravascular flow patterns determining WSS topological skeleton onto the vascular luminal surface.

# 2. Methods

## 2.1. Theoretical remarks

This section reports the background for a better understanding of the theory adopted in this study to demonstrate the analytical link between the topology of the WSS and SV in cardiovascular flows.

### *2.1.1. Wall shear stress vs. Surface Vorticity*

In a domain $\Omega \subset \mathbb{R}^3$ representing the lumen of a vessel (here fixed in time), considering blood as a generalized Newtonian fluid, the WSS $\boldsymbol{\tau}$ on the surface boundary $\partial\Omega$ is commonly defined as:

$$\boldsymbol{\tau} = \mathbb{P} \cdot (2\,\mu\,\boldsymbol{S}_{\partial\Omega} \cdot \boldsymbol{n}), \tag{1}$$

where $\mu$ is the dynamic viscosity, $\boldsymbol{n}$ is the unit vector normal to the surface boundary $\partial\Omega$, $\boldsymbol{S}_{\partial\Omega}$ is the strain rate tensor at the surface $\partial\Omega$, expressed in terms of the velocity vector gradient tensor $\nabla\boldsymbol{u}_{\partial\Omega}$:

$$\boldsymbol{S}_{\partial\Omega} = \frac{1}{2}(\nabla\boldsymbol{u}_{\partial\Omega} + \nabla\boldsymbol{u}_{\partial\Omega}^{T}), \tag{2}$$

and $\mathbb{P}$ is the tangential projection operator:

$$\mathbb{P} = \boldsymbol{I} - \boldsymbol{n} \otimes \boldsymbol{n}. \tag{3}$$

where $\boldsymbol{I}$ is the identity matrix. In equations (1) and (2) the subscript $\partial\Omega$ denotes the restriction of a quantity on the luminal surface of the vessel. As the velocity gradient tensor $\nabla\boldsymbol{u}_{\partial\Omega}$ at the surface $\partial\Omega$ can be expressed in terms of its symmetric ($\boldsymbol{S}_{\partial\Omega}$) and skew-symmetric ($\mathbf{W}_{\partial\Omega}$, the so-called spin tensor) parts:

$$\nabla\boldsymbol{u}_{\partial\Omega} = \boldsymbol{S}_{\partial\Omega} + \mathbf{W}_{\partial\Omega} = \frac{1}{2}(\nabla\boldsymbol{u}_{\partial\Omega} + \nabla\boldsymbol{u}_{\partial\Omega}{}^{T}) + \frac{1}{2}(\nabla\boldsymbol{u}_{\partial\Omega} - \nabla\boldsymbol{u}_{\partial\Omega}{}^{T}), \tag{4}$$

it follows that $\nabla\boldsymbol{u}_{\partial\Omega}^{T} = \boldsymbol{S}_{\partial\Omega} - \mathbf{W}_{\partial\Omega}$, and so the strain rate tensor $\boldsymbol{S}_{\partial\Omega}$ can be expressed in terms of spin tensor $\mathbf{W}_{\partial\Omega}$, i.e.:

$$\boldsymbol{S}_{\partial\Omega} = \nabla\boldsymbol{u}_{\partial\Omega}^{T} + \mathbf{W}_{\partial\Omega}. \tag{5}$$

By substituting eq. (5) in eq. (1), the WSS vector $\boldsymbol{\tau}$ can be expressed as:

$$\boldsymbol{\tau} = \mathbb{P} \cdot \left[2\,\mu\left(\nabla\boldsymbol{u}_{\partial\Omega}^{T} + \mathbf{W}_{\partial\Omega}\right) \cdot \boldsymbol{n}\right] = \mathbb{P} \cdot \left[2\,\mu\left(\nabla\boldsymbol{u}_{\partial\Omega}^{T} \cdot \boldsymbol{n} + \mathbf{W}_{\partial\Omega} \cdot \boldsymbol{n}\right)\right]. \tag{6}$$

For any generic vector $\boldsymbol{\xi}$, the spin tensor $\mathbf{W}_{\partial\Omega}$ satisfies the well-known relation:

$$2\mathbf{W}_{\partial\Omega} \cdot \boldsymbol{\xi} = \boldsymbol{\omega}_{\partial\Omega} \times \boldsymbol{\xi}, \tag{7}$$

where $\boldsymbol{\omega}_{\partial\Omega}$ is the SV, i.e., the vorticity on the luminal surface of the vessel. More details on the relation expressed by eq. (7) are presented in Appendix A.

According to eq. (7), and to the fact that the term $\nabla \boldsymbol{u}_{\partial\Omega}^{T} \cdot \boldsymbol{n}$ in eq. (6) is equal to zero being that $\partial\Omega$ is a fixed surface (rigid wall) [52], then eq. (6) can be reformulated as follows:

$$\boldsymbol{\tau} = \mathbb{P} \cdot ( \mu\, \boldsymbol{\omega}_{\partial\Omega} \times \boldsymbol{n} ). \tag{8}$$

Finally, according to the definition of the tangential projection operator $\mathbb{P}$ in eq. (3), eq. (8) can be reduced as follows:

$$\begin{aligned} \boldsymbol{\tau} &= (\boldsymbol{I} - \boldsymbol{n} \otimes \boldsymbol{n} ) \cdot ( \mu\, \boldsymbol{\omega}_{\partial\Omega} \times \boldsymbol{n} ) \\ &= (\mu\, \boldsymbol{\omega}_{\partial\Omega} \times \boldsymbol{n}) - (\boldsymbol{n} \otimes \boldsymbol{n}) \cdot ( \mu\, \boldsymbol{\omega}_{\partial\Omega} \times \boldsymbol{n} ) \\ &= (\mu\, \boldsymbol{\omega}_{\partial\Omega} \times \boldsymbol{n}) - [(\mu\, \boldsymbol{\omega}_{\partial\Omega} \times \boldsymbol{n}) \cdot \boldsymbol{n}]\boldsymbol{n} \\ &= \mu\, \boldsymbol{\omega}_{\partial\Omega} \times \boldsymbol{n}, \end{aligned} \tag{9}$$

where $(\mu\, \boldsymbol{\omega}_{\partial\Omega} \times \boldsymbol{n}) \cdot \boldsymbol{n}$ is equal to zero because vector $(\mu\, \boldsymbol{\omega}_{\partial\Omega} \times \boldsymbol{n})$ and unit vector $\boldsymbol{n}$ are orthogonal by construction.

A consequence of eq. (9) is that WSS and SV vectors form an orthogonal pair $(\boldsymbol{\tau}, \boldsymbol{\omega}_{\partial\Omega})$ on the luminal surface $\partial\Omega$. Moreover, based on eq. (9) the WSS vector $\boldsymbol{\tau}$ can be interpreted in terms of vorticity $\boldsymbol{\omega}$ in the near-wall, dictated by the shear viscosity and the no-slip condition. It must also be reminded here that fluid motion is characterized by the property that the vorticity $\boldsymbol{\omega}$ in the domain $\Omega$ is a solenoidal vector field. This property still applies to the SV vector $\boldsymbol{\omega}_{\partial\Omega}$ so that the following equation:

$$\nabla \cdot \boldsymbol{\omega}_{\partial\Omega} = 0, \tag{10}$$

is always satisfied on the luminal surface $\partial\Omega$.

Eq. (9) suggests that a relationship exists between the topological skeletons of $\boldsymbol{\tau}$ and $\boldsymbol{\omega}_{\partial\Omega}$. Clarifying the nature of this relationship would promote a deeper understanding of how the underlying blood flow vorticity field signatures shape topological skeleton features of the WSS,

which have been recently suggested as promoting factors of the onset and progression of vascular disease [6,23,24].

### *2.1.2. The topological skeleton of a vector field*

The analysis of the topological skeleton allows us to identify the essential structure of a vector field, offering a simple way to highlight its fundamental features. Based on dynamical system theory, the topological skeleton of a vector field is composed of fixed points and stable/unstable manifolds connecting them, where a fixed point $\boldsymbol{x}_{fp} \in \mathbb{R}^{\boldsymbol{n}}$ is a point where the vector field locally vanishes, and manifolds are directions along which the field lines condense or rarefy (Figure 1A).

Fixed points play a major role in shaping the topological skeleton structure, in consequence of their stable or unstable nature, defined as follows: a stable (unstable) fixed point is characterized by a sink (source) configuration, and it attracts (repels) the nearby field lines [14–16]. Moreover, fixed points can be classified as saddle points, nodes, foci or centres (Figure 1B): (i) a saddle point attracts and repels nearby field lines along different directions; (ii) a centre is encased within field lines forming closed loops; (iii) a stable/unstable node is characterized by converging/diverging field lines patterns; (iv) a stable/unstable focus is encased within converging/diverging and spiraling field lines (Figure 1B).

## 2.2. **Wall shear stress and Surface Vorticity fixed points**

In this section, we aim to analyze the relationship between fixed points of WSS vector $\boldsymbol{\tau}$ and SV vector $\boldsymbol{\omega}_{\partial\Omega}$, also investigating their nature and stability proprieties.

Let $(t_1, t_2, n)$ be a local coordinate system such that the unit vector $\boldsymbol{n}$ is normal to $\partial\Omega$, and thus $t_1$ and $t_2$ indicate the coordinates on the tangent plane, as illustrated in Figure 2. In general

terms, according to eq. (9) the WSS components can be expressed in the local coordinate system as a function of the SV components $\boldsymbol{\omega}_{\partial\Omega} = \left(\omega_{t_1}, \omega_{t_2}, \omega_n\right)$ (Figure 2) as follows:

$$\boldsymbol{\tau} = \left(\tau_{t_1}, \tau_{t_2}, 0\right) = \mu\boldsymbol{\omega}_{\partial\Omega} \times \boldsymbol{n} = \mu \det\begin{pmatrix} t_1 & t_2 & n \\ \omega_{t_1} & \omega_{t_2} & \omega_n \\ 0 & 0 & 1 \end{pmatrix} = (\mu\omega_{t_2}, -\mu\omega_{t_1}, 0). \quad (11)$$

From eq. (11) it follows that:

$$\forall\, \widetilde{\boldsymbol{x}} \in \partial\Omega : \boldsymbol{\tau}\left(\widetilde{\boldsymbol{x}}\right) = 0 \Rightarrow \boldsymbol{\omega}_{\partial\Omega}\left(\widetilde{\boldsymbol{x}}\right) = (0,0,\omega_n). \quad (12)$$

The main implication of eq. (12) is that if $\widetilde{\boldsymbol{x}} \in \partial\Omega$ is a fixed point of the WSS $\boldsymbol{\tau}$**,** this does not necessarily imply that $\widetilde{\boldsymbol{x}}$ is a fixed point of the SV $\boldsymbol{\omega}_{\partial\Omega}$: a fixed point of $\boldsymbol{\tau}$ is also fixed point for $\boldsymbol{\omega}_{\partial\Omega}$ *if and only if* $\omega_n = 0$. The subsections below deal with (i) the special case of flows where WSS and SV fixed points are coincident; and then (ii) the more general case where they may not be.

2.2.1. *Fixed points when the surface vorticity is purely tangential to the vessel's wall*

Let us first consider the case when the SV is purely tangential to the vessel wall, i.e.:

$$\exists\, \widehat{\boldsymbol{x}} \in \partial\Omega : \left(\boldsymbol{\omega}_{\partial\Omega} \cdot \boldsymbol{n}\right)_{\widehat{\boldsymbol{x}}} = 0. \quad (13)$$

Stricto sensu, eq. (13) is satisfied when the velocity vector in the near-wall region is tangent to the wall [53]. It is interesting to note that in fluid mechanics paradigms related to cardiovascular flows (e.g. fully developed flows like Hagen-Poiseuille and Womersley flows), the SV is always tangent to the wall, i.e. $\boldsymbol{\omega}_{\partial\Omega}$ satisfies eq. (13) everywhere on $\partial\Omega$.

In this case, it follows from eq. (12) that:

$$\forall\, \widetilde{\boldsymbol{x}} \in \partial\Omega : \boldsymbol{\tau}\left(\widetilde{\boldsymbol{x}}\right) = 0 \wedge \left(\boldsymbol{\omega}_{\partial\Omega} \cdot \boldsymbol{n}\right)_{\widetilde{\boldsymbol{x}}} = 0 \Rightarrow \boldsymbol{\omega}_{\partial\Omega}\left(\widetilde{\boldsymbol{x}}\right) = 0, \quad (14)$$

meaning that if $\widetilde{\boldsymbol{x}}$ is a fixed point of the $\boldsymbol{\tau}$ and if eq. (13) is satisfied at $\widetilde{\boldsymbol{x}} \in \partial\Omega$ , this necessarily implies that $\widetilde{\boldsymbol{x}}$ is also a fixed point of the $\boldsymbol{\omega}_{\partial\Omega}$ and vice versa. It should be noted here that this bijective

implication for fixed points when eq. (13) is satisfied does not imply that WSS and SV fixed points in $\widetilde{\boldsymbol{x}}$ share the same nature.

As the nature of fixed points markedly influence topological skeletons, an in-depth investigation is necessary at this stage to clarify the relationship between the nature of the $\boldsymbol{\tau}$ fixed point and of the $\boldsymbol{\omega}_{\partial\Omega}$ fixed point at $\widetilde{\boldsymbol{x}}$. To do that, it must be observed that in the case eq. (13) is satisfied at $\widetilde{\boldsymbol{x}} \in \partial\Omega$, the orthogonal pair $(\boldsymbol{\tau}, \boldsymbol{\omega}_{\partial\Omega})$ lies on the 2D space $\partial\Omega$. Thus, a two-dimensional analysis can be performed to identify and classify fixed points, determining their stability properties. Technically, the identification of fixed points can be carried out by computing the Poincaré index [54], a topological invariant index quantifying how many times a vector field rotates in the neighborhood of a point. The Poincaré index is equal to -1 at saddle point locations, 1 at node, focus or centre locations, and 0 otherwise. The Poincaré index allows identifying fixed points but does not provide information about fixed points' nature and stability. Instead, the classification of fixed points can be carried out by analyzing the sign of the eigenvalues $\lambda_{\mathrm{i}}$ of the Jacobian matrix $J$ of the vector field [16,53], as summarized in Table 1 (where a vector field lying in a 2D space has been considered).

**Table 1**. *Classification of fixed points based on the eigenvalues of the Jacobian matrix for a 2D vector field.*

| $\Lambda$ | **Fixed point** |
|---|---|
| $\boldsymbol{\lambda_1 < 0 < \lambda_2}$ | Saddle point |
| $\boldsymbol{\lambda_1, \lambda_2 > 0}$ | Unstable node |
| $\boldsymbol{\lambda_1, \lambda_2 < 0}$ | Stable node |
| $\boldsymbol{\lambda_{1,2} = \alpha \pm \beta i}$ | Unstable focus |
| $\boldsymbol{\lambda_{1,2} = -\alpha \pm \beta i}$ | Stable focus |
| $\boldsymbol{\lambda_{1,2} = \pm \beta i}$ | Centre |

In general, the eigenvalues $\lambda_{\mathrm{i}}$ of the Jacobian matrix $J$ are the roots of the characteristic polynomial $p_J(\lambda) = \det(J - \lambda I)$, where $I$ is the identity matrix. For a $2x2$ Jacobian matrix, the characteristic polynomial can be expressed in terms of trace and determinant as follows:

$$\lambda^2 - \mathrm{tr}(J)\lambda + \det(J) = 0, \tag{15}$$

where $\mathrm{tr}(J) = \lambda_1 + \lambda_2$ and $\det(J) = \lambda_1\lambda_2$.

According to eq. (15), the characteristic polynomial of the Jacobian matrix of $\boldsymbol{\tau}$ at $\tilde{\boldsymbol{x}} \in \partial\Omega$ can be expressed as:

$$p_{J(\boldsymbol{\tau})_{\tilde{\boldsymbol{x}}}}(\lambda) = \lambda^2 - \mathrm{tr}(J(\boldsymbol{\tau})_{\tilde{\boldsymbol{x}}})\lambda + \det(J(\boldsymbol{\tau})_{\tilde{\boldsymbol{x}}}) = 0, \tag{16}$$

where:

$$J(\tau)_{\tilde{\boldsymbol{x}}} = \begin{pmatrix} \dfrac{\partial \tau_{t_1}}{\partial t_1} & \dfrac{\partial \tau_{t_1}}{\partial t_2} \\ \dfrac{\partial \tau_{t_2}}{\partial t_1} & \dfrac{\tau_{t_2}}{\partial t_2} \end{pmatrix}_{\tilde{\boldsymbol{x}}} = \mu \begin{pmatrix} \dfrac{\partial \omega_{t_2}}{\partial t_1} & \dfrac{\partial \omega_{t_2}}{\partial t_2} \\ -\dfrac{\partial \omega_{t_1}}{\partial t_1} & -\dfrac{\partial \omega_{t_1}}{\partial t_2} \end{pmatrix}_{\tilde{\boldsymbol{x}}}, \tag{17}$$

is a symmetric matrix because it follows from eq. (10) that $\frac{\partial \omega_{t_2}}{\partial t_2} = -\frac{\partial \omega_{t_1}}{\partial t_1}$. Similarly, based on eq. (10) and on the fact that $\mathrm{tr}(J(\boldsymbol{\omega}_{\partial\Omega})_{\tilde{\boldsymbol{x}}}) = \nabla \cdot \boldsymbol{\omega}_{\partial\Omega} = 0$, the characteristic polynomial of the Jacobian matrix of the $\boldsymbol{\omega}_{\partial\Omega}$ at $\tilde{\boldsymbol{x}} \in \partial\Omega$, can be expressed as:

$$p_{J(\boldsymbol{\omega}_{\partial\Omega})_{\tilde{\boldsymbol{x}}}} = \lambda^2 + \det(J(\boldsymbol{\omega}_{\partial\Omega})_{\tilde{\boldsymbol{x}}}) = 0. \tag{18}$$

Considering that (i) $\det(J(\boldsymbol{\omega}_{\partial\Omega})) = \frac{\det(J(\boldsymbol{\tau}))}{\mu^2}$ by construction, and that (ii) $\det(J) = \lambda_1\lambda_2$, it follows that:

- if $\det(J(\boldsymbol{\omega}_{\partial\Omega})_{\tilde{\boldsymbol{x}}}) = \frac{\det(J(\boldsymbol{\tau})_{\tilde{\boldsymbol{x}}})}{\mu^2} < 0$, then eigenvalues are real numbers but with different signs and thus the fixed point $\tilde{\boldsymbol{x}}$ is a saddle point (Table 1) for both $\boldsymbol{\omega}_{\partial\Omega}$ and $\boldsymbol{\tau}$ (Figure 3A);
- if $\det(J(\boldsymbol{\omega}_{\partial\Omega})_{\tilde{\boldsymbol{x}}}) = \frac{\det(J(\boldsymbol{\tau})_{\tilde{\boldsymbol{x}}})}{\mu^2} > 0$, then eigenvalues are pure imaginary numbers for $\boldsymbol{\omega}_{\partial\Omega}$ and real numbers with the same sign for $\boldsymbol{\tau}$ (as a consequence of symmetry of the Jacobian

matrix of $\boldsymbol{\tau}$) and thus fixed point $\widetilde{\boldsymbol{x}}$ is a centre for $\boldsymbol{\omega}_{\partial\Omega}$ (Table 1, Figure 3A) and a stable/instable node for $\boldsymbol{\tau}$, according to the sign of quantities $\mathrm{tr}(J(\boldsymbol{\tau})_{\widetilde{\boldsymbol{x}}})^2 - 4\det(J(\boldsymbol{\tau})_{\widetilde{\boldsymbol{x}}})$ and $\mathrm{tr}(J(\boldsymbol{\tau})_{\widetilde{\boldsymbol{x}}})$ (Table 1, Figure 3A).

The complete stability analysis of the fixed point $\widetilde{\boldsymbol{x}} \in \partial\Omega$ of SV and WSS when eq. (13) is satisfied (i.e., when the $\boldsymbol{\omega}_{\partial\Omega}$ is tangent to the luminal surface), is summarized in Figure 3A.

2.2.2. *Fixed points when the surface vorticity is not purely tangential to the vessel's wall*

Let us now consider the case when eq. (13) is not satisfied, i.e.:

$$\exists\, \widehat{\boldsymbol{x}} \in \partial\Omega : \ (\boldsymbol{\omega}_{\partial\Omega} \cdot \boldsymbol{n})_{\widehat{\boldsymbol{x}}} \neq 0. \tag{19}$$

From eq. (12) it follows that:

$$\forall\, \widehat{\boldsymbol{x}} \in \partial\Omega : \boldsymbol{\tau}(\widehat{\boldsymbol{x}}) = 0 \ \wedge \ (\boldsymbol{\omega}_{\partial\Omega} \cdot \boldsymbol{n})_{\widehat{\boldsymbol{x}}} \neq 0 \Rightarrow \ \boldsymbol{\omega}_{\partial\Omega}(\widehat{\boldsymbol{x}}) = \omega_n \boldsymbol{n}, \tag{20}$$

meaning that if $\widehat{\boldsymbol{x}}$ is a fixed point of the $\boldsymbol{\tau}$ and if $\boldsymbol{\omega}_{\partial\Omega}$ satisfies eq. (19) at $\widehat{\boldsymbol{x}} \in \partial\Omega$, then it follows that (i) $\widehat{\boldsymbol{x}}$ cannot be a fixed point for $\boldsymbol{\omega}_{\partial\Omega}$, and (ii) the SV is purely normal to the wall. This contemplates that a not-null vorticity flux normal to the wall $\sigma_n$ might be established as a consequence of the markedly three-dimensional flow field observable within complex vascular anatomies, in infinitesimal neighborhoods of flow disturbances. In detail, the vorticity flux $\sigma_n$ normal to the luminal surface $\partial\Omega$ can be expressed as:

$$\sigma_n = -\nu\, \nabla_\pi \cdot \boldsymbol{\omega}_{\partial\Omega}\,, \tag{21}$$

where $\nu$ is the kinematic viscosity and $\nabla_\pi$ is the surface gradient tangent to the luminal surface $\partial\Omega$.

The classification of fixed points $\widehat{\boldsymbol{x}} \in \partial\Omega$ of $\boldsymbol{\tau}$, also in this case, can be performed by solving the characteristic polynomial of the Jacobian matrix of $\boldsymbol{\tau}$ at $\widehat{\boldsymbol{x}}$ and by analyzing the eigenvalues:

$$p_{J(\boldsymbol{\tau})_{\hat{\boldsymbol{x}}}}(\lambda) = \lambda^2 - \mathrm{tr}(J(\boldsymbol{\tau})_{\hat{\boldsymbol{x}}})\lambda + \det\left(J(\boldsymbol{\tau})_{\hat{\boldsymbol{x}}}\right) = 0. \quad (22)$$

Contrary to the case where $\boldsymbol{\omega}_{\partial\Omega}$ is purely tangent to the luminal surface $\partial\Omega$, characterized by a symmetric Jacobian matrix $J(\boldsymbol{\tau})_{\tilde{\boldsymbol{x}}}$ (as shown in eq. (17)), a consequence of having $\sigma_n(\hat{\boldsymbol{x}}) \neq 0$ is that $J(\boldsymbol{\tau})_{\hat{\boldsymbol{x}}}$ is no longer a symmetric matrix, since $\frac{\partial \omega_{t_2}}{\partial t_2} + \frac{\partial \omega_{t_1}}{\partial t_1} = \nabla_\pi \cdot \boldsymbol{\omega}_{\partial\Omega} \neq 0$. In this case, we have:

- if $\det(J(\boldsymbol{\tau})_{\hat{\boldsymbol{x}}}) < 0$, eigenvalues are real numbers but with different sign and thus $\tilde{\boldsymbol{x}}$ is a saddle point for $\boldsymbol{\tau}$ (Table 1, Figure 3B);
- if $\det(J(\boldsymbol{\tau})_{\hat{\boldsymbol{x}}}) > 0$, eigenvalues can be complex and conjugate or real numbers with the same sign and thus $\tilde{\boldsymbol{x}}$ can be a stable/instable focus or node for $\boldsymbol{\tau}$, according to the sign of quantities $\mathrm{tr}\left(J(\boldsymbol{\tau})_{\hat{\boldsymbol{x}}}\right)^2 - 4\det\left(J(\boldsymbol{\tau})_{\hat{\boldsymbol{x}}}\right)$ and $\mathrm{tr}(J(\boldsymbol{\tau})_{\hat{\boldsymbol{x}}})$ (Table 1, Figure 3B).

The complete stability analysis of the fixed points of WSS when the SV is purely normal to the wall is summarized in Figure 3B.

## 2.3. **Computational Hemodynamics**

Intracranial aneurysm models from the Toronto Western Hospital aneurysm clinic were considered in this study to test results from the theoretical analysis. These cases were provided under Toronto Western Hospital's Research Ethics Board Approval (REB #19-5823), which authorizes research analysis and publication of anonymized and de-identified patient imaging data from their aneurysm clinic. Exhaustive details regarding geometry reconstruction, meshing strategy and CFD settings have been extensively described in previous studies [15,55,56]. In brief, 3D lumen geometries were reconstructed from 3D rotational angiography and 4D computed tomography angiography, and segmented using a morphological gradient-based watershed method [57]. Tetrahedral meshes were generated by using VMTK software, and high-fidelity computational fluid dynamics simulations were

performed using a minimally dissipative solver developed within the open-source finite-element-method library FEniCS [58]. Fully developed Womersley velocity profiles were applied at inlet sections, and outflow divisions were based on a splitting method presented elsewhere [55]. The Reynolds number (a dimensionless fluid dynamic quantity given by the ratio between inertial and viscous forces) at peak flow rate at the inflow section was 359 for model A1 and 337 for model A2 [56].

The identification and classification of fixed points at the luminal surface of intracranial aneurysm models is performed by computing the Poincaré index and the eigenvalues of the Jacobian matrix $J$ as exhaustively detailed elsewhere [15]. Here, however, a thorough characterization of the complex volumetric vortex structures in the intracranial aneurysm models was desired, since the final aim is the identification of those intravascular fluid structures whose interaction with the vessel wall determine WSS and SV topological features on the luminal surface. To achieve this, the CFD velocity data were used to implement the recently proposed vorticity vector decomposition [59]: according to this approach, the vorticity vector can be decomposed into a purely rotational contribution $\boldsymbol{R}$ representing the rigid-body rotation, and a non-rotational contribution, which is related to shear [60,61]. Referring the reader to [59,60,62] for the basic theory underpinning such vorticity vector decomposition, here we focused on the rotational part $\boldsymbol{R}$ of vorticity, which can be defined as [59]:

$$\boldsymbol{R} = R\boldsymbol{r} = \left(\boldsymbol{\omega}\cdot\boldsymbol{r} - \sqrt{(\boldsymbol{\omega}\cdot\boldsymbol{r})^2 - 4\lambda_{ci}^2}\right)\boldsymbol{r}\,, \tag{23}$$

where $\boldsymbol{r}$ is the unit real eigenvector of the velocity gradient tensor $\nabla\boldsymbol{u}$, and $\lambda_{ci}$ is the imaginary part of the complex conjugate eigenvalues of $\nabla\boldsymbol{u}$**.** Different from other vortex identification methods such as Q-criterion, $\lambda_2$ or $\lambda_{ci}$, $\boldsymbol{R}$ provides both the vortex local rotational axis and the rotational strength, being free from shear contamination [63].

# 3. Results

## 3.1. Wall shear stress and Surface Vorticity fixed points

Instantaneous SV and WSS distributions at mid systolic acceleration point with their fixed points and field lines on the luminal surface of two explanatory intracranial aneurysm CFD models are presented in Figure 4 (model A1) and in Figure 5 (model A2). According to the developed theory summarized in Figure 3, it clearly emerges from Figures 4 and 5 that: (i) $(\boldsymbol{\tau}, \boldsymbol{\omega}_{\partial\Omega})$ form an orthogonal pair on the luminal surface $\partial\Omega$, and (ii) $\boldsymbol{\omega}_{\partial\Omega}$ fixed points are always $\boldsymbol{\tau}$ fixed points, but not vice versa. Looking at the luminal surface of aneurysmal sac of model A1, many theoretical topological feature configurations exposed by our theory appear, i.e. one saddle point for both $\boldsymbol{\tau}$ and $\boldsymbol{\omega}_{\partial\Omega}$, one unstable node for $\boldsymbol{\tau}$ which is a centre for $\boldsymbol{\omega}_{\partial\Omega}$ , one stable focus for $\boldsymbol{\tau}$ which is not a fixed point for $\boldsymbol{\omega}_{\partial\Omega}$ (Figure 4A), and one saddle point for $\boldsymbol{\tau}$ which is not a fixed point for $\boldsymbol{\omega}_{\partial\Omega}$ (Figure 4B). Interestingly, it can be noted that the unstable and stable manifolds starting from the $\boldsymbol{\tau}$ saddle point (i.e., the critical lines attracting and repelling neighbouring fluid elements depicted in Figure 1A) are rotated with respect to the unstable and stable manifolds starting from the $\boldsymbol{\omega}_{\partial\Omega}$ saddle point. Moreover, we can appreciate that the diverging WSS pattern around the unstable node for $\boldsymbol{\tau}$ colocalizes with SV field lines forming closed loops encasing the centre for $\boldsymbol{\omega}_{\partial\Omega}$ (Figure 4A), confirming that the SV must be purely tangential to the luminal surface in a neighborhood of the point. In addition, it can be observed how the SV presents converging spiraling field lines where a stable focus for $\boldsymbol{\tau}$ has been identified (Figure 4A), confirming that the SV $\boldsymbol{\omega}_{\partial\Omega}$ must be purely normal to the wall at that point, to not violate eq. (10).

The analysis of model A2 in Figure 5 allows us to present a case that is covered by theory but did not occur on the luminal surface of model A1. In fact, in the case of model A2, two fixed points that are saddle point for both $\boldsymbol{\tau}$ and $\boldsymbol{\omega}_{\partial\Omega}$ (Figure 5), one unstable node for $\boldsymbol{\tau}$ (Fig 5) and one stable

focus for $\boldsymbol{\tau}$ that are not fixed points for $\boldsymbol{\omega}_{\partial\Omega}$ (Figure 5) are identified on the luminal surface of the aneurysmal sac. Contrarily to model A1, the source configuration of the WSS field lines around the unstable node for $\boldsymbol{\tau}$ colocalizes with converging spiraling SV lines (Figure 5), indicating that a not null vorticity flux $\sigma_n$ normal to the wall must occur, to not violate eq. (10) and as predicted by theory.

### 3.2. Identifying the link between fixed points and intravascular fluid structures

To clarify if fluid-mechanistic cause-effect relationships can be identified between WSS topological features and intravascular fluid structures, flow visualizations based on instantaneous streamlines and on the rotational part of vorticity $\boldsymbol{R}$ (as introduced in eq. (23)) inside the explanatory intracranial aneurysm models A1 (Figure 6) and A2 (Figure 7) were adopted.

From Figure 6, it emerges that: (i) a stable focus for $\boldsymbol{\tau}$ is generated by a highly rotational fluid structure emanating from the wall (as highlighted by the combined instantaneous velocity streamlines, $\boldsymbol{R}$ magnitude isosurfaces visualization in Figure 6, and $\boldsymbol{R}$ vector directions in Figure 8); (ii) a saddle point for both $\boldsymbol{\tau}$ and $\boldsymbol{\omega}_{\partial\Omega}$ attracts and repels velocity field lines in the near-wall region (as highlighted by the visualization of instantaneous velocity streamlines in the near-wall region), while no vortex structures are present in a neighborhood of the fixed point location; (iii) an unstable node for $\boldsymbol{\tau}$, which is also a centre for $\boldsymbol{\omega}_{\partial\Omega}$, is characterized by diverging near-wall tangential instantaneous velocity streamlines, with non-rotating fluid structures interacting with the wall; (iv) a saddle point for $\boldsymbol{\tau}$ which is not a fixed point for $\boldsymbol{\omega}_{\partial\Omega}$ is generated by the interaction with the wall of two counter-rotating fluid structures (as highlighted by the isosurfaces of $\boldsymbol{R}$ magnitude in Figure 6, and by the near-wall $\boldsymbol{R}$ vector directions, indicating the axis of rotation of the vortex structures, presented in Figure 8).

Regarding model A2, Figure 7 clearly shows, according to the theory and to what was observed in model A1, that (i) a stable focus for $\boldsymbol{\tau}$ originates from the interaction between a rotational (emanating from the wall) fluid structure and the wall; (ii) a saddle point for both $\boldsymbol{\tau}$ and

$\boldsymbol{\omega}_{\partial\Omega}$ attracts and repels velocity field lines in the near-wall region; and (iii) an unstable node for $\boldsymbol{\tau}$, which is not a fixed point for $\boldsymbol{\omega}_{\partial\Omega}$, is the consequence of non-rotational fluid structure impinging to the wall (in this case generated by the impingement of a non-rotational jet flow entering the aneurysmal dome).

## 4. Discussion

Unveiling the mechanisms of flow disturbances in vascular disease is crucial for the advancement of our understanding of *disease* mechanisms, the identification of risk factors, the development of effective therapeutic strategies, and the enhancement of diagnostic technologies. Despite the efforts expended and the documented progress, the definition of cardiovascular flow disturbances remains elusive, severely hampering the clear interpretation of the role of local hemodynamics in vascular pathophysiology, as well as the consequent clinical impact. With the final purpose of deciphering the nature of the local interactions at the interface between cardiovascular structures and flows, and promoting the unambiguous identification of the hemodynamic patterns involved in vascular pathophysiology, a unified theory was presented in this study to demonstrate that the WSS topological skeleton on the luminal surface of a vessel is "sculptured" by specific intravascular fluid structures, and that this relationship between near-wall *vs.* bulk flow can be expressed in terms of blood flow vorticity. In detail, here it was theoretically demonstrated that: (i) all SV fixed points on the luminal surface must also be WSS fixed points, but different in nature and stability; (ii) contrariwise, a WSS fixed point is not necessarily a fixed point for SV. In the former case, we have shown that the WSS fixed point is the consequence of flow patterns where only shear contributes to vorticity (i.e. where the contribution of $\boldsymbol{R}$ to the vorticity, eq. (23), is negligible). In the latter case, the SV must be solely normal to the luminal surface with an associated not-null vorticity flux, which in turn implies that the WSS fixed point is a consequence of flow impingement to or emanation from the vessel wall. Moreover, high-fidelity CFD data in intracranial aneurysm models confirmed the

emerged theoretical links between WSS and SV topology on the luminal surface, helping to clarify the cause-effect relationships between WSS topological features and intravascular fluid structures.

A summary of the main findings of this study is presented in Figure 9. Briefly, a stable/unstable node for the WSS can have a twofold nature, namely, it can be a centre fixed point for the SV if it is determined by the interaction of the vessel wall with flow patterns characterized by solely shear viscosity (Figure 6), or it can be the consequence of a non-rotational fluid structure emanating from/impinging to the wall (Figure 7) and it is not a SV fixed point. Similarly, a WSS saddle point can also be a SV saddle point, with an associated 90 degree manifold rotation in the topological skeleton (Figures 6 and 7) as described by theory (eq. 9), or it can be generated by the presence of two counter-rotating fluid structures in the near-wall region (Figure 6) and it is not a SV fixed point.

Interestingly, a WSS stable/unstable focus cannot be a SV fixed point and it is necessarily generated by a rotational fluid structure emanating from/impinging to the wall (Figure 6).

Among the main fluid mechanical implications, the proposed analysis provides a method to unambiguously distinguish WSS fixed points on the luminal surface originating from the interaction between the vessel wall and solely shear vorticity, non-rotational or highly rotational fluid structures. The presented analysis is also of potential mechanobiological relevance, because an interaction of the luminal surface with solely shear flow rather than with rotational or non-rotational fluid structures differently shapes the WSS topological skeleton, which has emerged as a remarkable predictor of vascular disease [6,8,23,24]. In this sense, linking WSS topological features with peculiar fluid structures on a theoretical basis will allow us to unambiguously define what can be considered flow disturbance in relation to a specific pathology or in relation to a specific vessel. The practical implications are that the here proposed analysis could provide a biomechanical tool to evaluate/predict the impact of cardiovascular surgical interventions or devices implantation on the near wall hemodynamics. Moreover, the application of the proposed theory could become a useful

tool supporting cardiovascular devices design and optimization. As an example, which is linked to the case study presented in our manuscript, we remind here that treatments of intracranial aneurysms involve the implantation of flow diverters or aneurysms coiling. Both the solutions aim at imparting a flow reduction within the aneurysmal sac, promoting progressive aneurysm thrombosis with subsequent healing of the disease. Since inaccurate flow diverter positioning and coiling both reduce the chances of sufficient exclusion of the aneurysmal sac from the circulation [64,65], an in-depth knowledge of the hemodynamic changes occurring in intracranial aneurysms after flow diverter or coiling deployment is essential to evaluate their efficacy, and a flow topology-based analysis as the one proposed in this study might be adopted to clarify the reasons why devices implantation fail and to guide devices optimization, facilitating treatment and predicting treatment outcomes.

The presented approach might suffer from the limitation that the emerged theoretical remarks could manifest sensitivity to CFD resolution, idealization, and assumptions. Although this remains to be determined for different cardiovascular territories and pathologies, results from the high-fidelity CFD simulations adopted in this study are in concordance with the theoretical considerations, and are further confirmation that the WSS topological skeleton analysis is feasible on computational hemodynamics models [14,15,23,24].

## 5. Conclusion

The theoretical framework presented in this study provides a key to interpreting and efficiently clarifying the cause-effect relationships linking intravascular fluid structures with WSS topological skeleton on the luminal surface of a vessel, thus allowing unambiguous identification of cardiovascular flow disturbances towards elucidating their mechanistic links with biological adverse events as well as with clinical observations. With the proposed theory-based interpretive key, future

studies exploring how WSS fixed points and manifolds generated by different intravascular flow patterns impact vascular mechanobiology are warranted and encouraged.

## Acknowledgments

The author V.M. is supported by the project NODES which has received funding from the MUR – M4C2 1.5 of PNRR funded by the European Union - NextGenerationEU (Grant agreement no. ECS00000036). The authors D.G. and K.C. acknowledge the support of «ASSOCIATE» project (code 2022L7KK7L) – funded by European Union – Next Generation EU within the PRIN 2022 program (D.D. 104 - 02/02/2022 Ministero dell'Università e della Ricerca).

## Author declarations

*Conflict of interest*

The authors have no conflicts to disclose.

*Author contributions*

Conceptualization: V.M., D.G., and U.M.; Data curation: V.M, K.C., and D.A.S; Formal analysis: V.M and U.M.; Methodology: V.M., D.G., and U.M.; Investigation: V.M and U.M.; Visualization: V.M and K.C.; Supervision: U.M.; Writing–original draft: V.M., D.G., D.A.S, and U.M.; Writing–review and editing: V.M., D.G., K.C., D.A.S, and U.M.

*Data Availability Statement*

The data that support the findings of this study are available from the corresponding author upon reasonable request.

## APPENDIX A

Let us consider the spin tensor $\mathbf{W}_{\partial\Omega}$, defined as:

$$\mathbf{W}_{\partial\Omega} = \frac{1}{2}(\nabla \boldsymbol{u}_{\partial\Omega} - \nabla \boldsymbol{u}_{\partial\Omega}{}^{T}) = \frac{1}{2}\begin{pmatrix} \frac{\partial u_x}{\partial x} & \frac{\partial u_x}{\partial y} & \frac{\partial u_x}{\partial z} \\ \frac{\partial u_y}{\partial x} & \frac{\partial u_y}{\partial y} & \frac{\partial u_y}{\partial z} \\ \frac{\partial u_z}{\partial x} & \frac{\partial u_z}{\partial y} & \frac{\partial u_z}{\partial z} \end{pmatrix} - \begin{pmatrix} \frac{\partial u_x}{\partial x} & \frac{\partial u_y}{\partial x} & \frac{\partial u_z}{\partial x} \\ \frac{\partial u_x}{\partial y} & \frac{\partial u_y}{\partial y} & \frac{\partial u_z}{\partial y} \\ \frac{\partial u_x}{\partial z} & \frac{\partial u_y}{\partial z} & \frac{\partial u_z}{\partial z} \end{pmatrix}, \qquad \text{(A1)}$$

and let $\boldsymbol{\xi}$ be a generic vector $\boldsymbol{\xi} = (\xi_x, \xi_y, \xi_z)$. The inner product between the spin tensor and the vector $\boldsymbol{\xi}$ is given by:

$$\mathbf{W}_{\partial\Omega} \cdot \boldsymbol{\xi} = \frac{1}{2}\begin{pmatrix} 0 & \frac{\partial u_x}{\partial y} - \frac{\partial u_y}{\partial x} & \frac{\partial u_x}{\partial z} - \frac{\partial u_z}{\partial x} \\ \frac{\partial u_y}{\partial x} - \frac{\partial u_x}{\partial y} & 0 & \frac{\partial u_y}{\partial z} - \frac{\partial u_z}{\partial y} \\ \frac{\partial u_z}{\partial x} - \frac{\partial u_x}{\partial z} & \frac{\partial u_z}{\partial y} - \frac{\partial u_y}{\partial z} & 0 \end{pmatrix} \cdot \begin{pmatrix} \xi_x \\ \xi_y \\ \xi_z \end{pmatrix}$$

$$= \begin{pmatrix} \left(\frac{\partial u_x}{\partial y} - \frac{\partial u_y}{\partial x}\right)\xi_y + \left(\frac{\partial u_x}{\partial z} - \frac{\partial u_z}{\partial x}\right)\xi_z \\ \left(\frac{\partial u_y}{\partial x} - \frac{\partial u_x}{\partial y}\right)\xi_x + \left(\frac{\partial u_y}{\partial z} - \frac{\partial u_z}{\partial y}\right)\xi_z \\ \left(\frac{\partial u_z}{\partial x} - \frac{\partial u_x}{\partial z}\right)\xi_x + \left(\frac{\partial u_z}{\partial y} - \frac{\partial u_y}{\partial z}\right)\xi_y \end{pmatrix} = \frac{1}{2}\begin{pmatrix} -\omega_z\xi_y + \omega_y\xi_z \\ \omega_z\xi_x - \omega_x\xi_z \\ -\omega_y\xi_x + \omega_x\xi_y \end{pmatrix} \qquad \text{(A2)}$$

$$= \frac{1}{2}\begin{pmatrix} \omega_y\xi_z - \omega_z\xi_y \\ \omega_z\xi_x - \omega_x\xi_z \\ \omega_x\xi_y - \omega_y\xi_x \end{pmatrix} = \frac{1}{2}\,\boldsymbol{\omega}_{\partial\Omega} \times \boldsymbol{\xi}.$$

Eq. (A2) is the well-known relation expressed in eq. (7).

## References


[1] U. Morbiducci, A.M. Kok, B.R. Kwak, P.H. Stone, D.A. Steinman, and J.J. Wentzel, "Atherosclerosis at arterial bifurcations: Evidence for the role of haemodynamics and geometry," Thromb. Haemost. **115**(3), 484–492 (2016).

[2] C.K. Zarins, D.P. Giddens, B.K. Bharadvaj, V.S. Sottiurai, R.F. Mabon, and S. Glagov, "Carotid bifurcation atherosclerosis. Quantitative correlation of plaque localization with flow velocity profiles and wall shear stress.," Circ. Res. **53**(4), 502–514 (1983).

[3] D.N. Ku, D.P. Giddens, C.K. Zarins, and S. Glagov, "Pulsatile flow and atherosclerosis in the human carotid bifurcation. Positive correlation between plaque location and low oscillating shear stress.," Arteriosclerosis **5**(3), 293–302 (1985).

[4] C.G. Caro, J.M. Fitz-Gerald, and R.C. Schroter, "Atheroma and arterial wall shear. Observation, correlation and proposal of a shear dependent mass transfer mechanism for atherogenesis.," Proc. R. Soc. London. Ser. B, Biol. Sci. **177**(1046), 109–159 (1971).

[5] B.R. Kwak, M. Bäck, M.-L. Bochaton-Piallat, G. Caligiuri, M.J.A.P. Daemen, P.F. Davies, I.E. Hoefer, P. Holvoet, H. Jo, R. Krams, S. Lehoux, C. Monaco, S. Steffens, R. Virmani, C. Weber, J.J. Wentzel, and P.C. Evans, "Biomechanical factors in atherosclerosis: mechanisms and clinical implications," Eur. Heart J. **35**(43), 3013-3020d (2014).

[6] A. Candreva, M. Pagnoni, M.L. Rizzini, T. Mizukami, E. Gallinoro, V. Mazzi, D. Gallo, D. Meier, T. Shinke, J.-P. Aben, S. Nagumo, J. Sonck, D. Munhoz, S. Fournier, E. Barbato, W. Heggermont, S. Cook, C. Chiastra, U. Morbiducci, B. De Bruyne, O. Muller, and C. Collet, "Risk of myocardial infarction based on endothelial shear stress analysis using coronary angiography.," Atherosclerosis **342**, 28–35 (2022).

[7] F.J.H. Gijsen, J.J. Wentzel, A. Thury, F. Mastik, J.A. Schaar, J.C.H. Schuurbiers, C.J. Slager, W.J. van der Giessen, P.J. de Feyter, A.F.W. van der Steen, and P.W. Serruys, "Strain distribution over plaques in human coronary arteries relates to shear stress.," Am. J. Physiol. Heart Circ. Physiol. **295**(4), H1608-14 (2008).

[8] G. De Nisco, E.M.J. Hartman, E. Torta, J. Daemen, C. Chiastra, D. Gallo, U. Morbiducci, and J.J. Wentzel, "Predicting Lipid-Rich Plaque Progression in Coronary Arteries Using Multimodal Imaging and Wall Shear Stress Signatures," Arterioscler. Thromb. Vasc. Biol. **0**(0), (2024).

[9] A. Arzani, A.M. Gambaruto, G. Chen, and S.C. Shadden, "Wall shear stress exposure time: a Lagrangian measure of near-wall stagnation and concentration in cardiovascular flows.," Biomech. Model. Mechanobiol. **16**(3), 787–803 (2017).

[10] N. Baeyens, C. Bandyopadhyay, B.G. Coon, S. Yun, and M.A. Schwartz, "Endothelial fluid shear stress sensing in vascular health and disease.," J. Clin. Invest. **126**(3), 821–828 (2016).

[11] V. Peiffer, S.J. Sherwin, and P.D. Weinberg, "Does low and oscillatory wall shear stress correlate spatially with early atherosclerosis? A systematic review.," Cardiovasc. Res. **99**(2), 242–250 (2013).

[12] D. Gallo, P.B. Bijari, U. Morbiducci, Y. Qiao, Y.J. Xie, M. Etesami, D. Habets, E.G. Lakatta, B.A. Wasserman, and D.A. Steinman, "Segment-specific associations between local haemodynamic and imaging markers of early atherosclerosis at the carotid artery: an in vivo human study.," J. R. Soc. Interface **15**(147), (2018).

[13] A.M. Kok, D.S. Molony, L.H. Timmins, Y.-A. Ko, E. Boersma, P. Eshtehardi, J.J. Wentzel, and H.

Samady, “The influence of multidirectional shear stress on plaque progression and composition changes in human coronary arteries.,” EuroIntervention J. Eur. Collab. with Work. Gr. Interv. Cardiol. Eur. Soc. Cardiol. **15**(8), 692–699 (2019).

[14] A. Arzani, and S.C. Shadden, “Wall shear stress fixed points in cardiovascular fluid mechanics,” J. Biomech. **73**, 145–152 (2018).

[15] V. Mazzi, D. Gallo, K. Calò, M. Najafi, M.O. Khan, G. De Nisco, D.A. Steinman, and U. Morbiducci, “A Eulerian method to analyze wall shear stress fixed points and manifolds in cardiovascular flows,” Biomech. Model. Mechanobiol. **19**(5), 1403–1423 (2020).

[16] V. Mazzi, U. Morbiducci, K. Calò, G. De Nisco, M. Lodi Rizzini, E. Torta, G.C.A. Caridi, C. Chiastra, and D. Gallo, “Wall Shear Stress Topological Skeleton Analysis in Cardiovascular Flows: Methods and Applications,” Mathematics **9**(7), (2021).

[17] V. Goodarzi Ardakani, X. Tu, A.M. Gambaruto, I. Velho, J. Tiago, A. Sequeira, and R. Pereira, “Near-Wall Flow in Cerebral Aneurysms,” Fluids **4**(2), 89 (2019).

[18] H.J. Carpenter, M.H. Ghayesh, A.C. Zander, and P.J. Psaltis, “Effect of coronary artery dynamics on the wall shear stress vector field topological skeleton in fluid–structure interaction analyses,” Int. J. Mech. Syst. Dyn. **3**(1), 48–57 (2023).

[19] P.G. Ledda, T. Rossi, M.G. Badas, and G. Querzoli, “Can wall shear-stress topology predict proliferative vitreoretinopathy localization following pars plana vitrectomy?,” J. Biomech. **162**, 111914 (2024).

[20] E. Tsolaki, P. Corso, R. Zboray, J. Avaro, C. Appel, M. Liebi, S. Bertazzo, P.P. Heinisch, T. Carrel, D. Obrist, and I.K. Herrmann, “Multiscale multimodal characterization and simulation of structural alterations in failed bioprosthetic heart valves.,” Acta Biomater. **169**, 138–154 (2023).

[21] C. Chiastra, V. Mazzi, M. Lodi Rizzini, K. Calò, A. Corti, A. Acquasanta, G. De Nisco, D. Belliggiano, E. Cerrato, D. Gallo, and U. Morbiducci, “Coronary Artery Stenting Affects Wall Shear Stress Topological Skeleton,” J. Biomech. Eng. **144**(6), (2022).

[22] G. De Nisco, P. Tasso, K. Calò, V. Mazzi, D. Gallo, F. Condemi, S. Farzaneh, S. Avril, and U. Morbiducci, “Deciphering ascending thoracic aortic aneurysm hemodynamics in relation to biomechanical properties,” Med. Eng. Phys. **82**, 119–129 (2020).

[23] U. Morbiducci, V. Mazzi, M. Domanin, G. De Nisco, C. Vergara, D.A. Steinman, and D. Gallo, “Wall Shear Stress Topological Skeleton Independently Predicts Long-Term Restenosis After Carotid Bifurcation Endarterectomy,” Ann. Biomed. Eng. **48**(12), 2936–2949 (2020).

[24] V. Mazzi, G. De Nisco, A. Hoogendoorn, K. Calò, C. Chiastra, D. Gallo, D.A. Steinman, J.J. Wentzel, and U. Morbiducci, “Early Atherosclerotic Changes in Coronary Arteries are Associated with Endothelium Shear Stress Contraction/Expansion Variability,” Ann. Biomed. Eng., (2021).

[25] M. Mahmoudi, A. Farghadan, D. McConnell, A.J. Barker, J.J. Wentzel, M.J. Budoff, and A. Arzani, “The Story of Wall Shear Stress in Coronary Artery Atherosclerosis: Biochemical Transport and Mechanotransduction,” J. Biomech. Eng., (2020).

[26] V. Mazzi, G. De Nisco, K. Calò, C. Chiastra, J. Daemen, D.A. Steinman, J.J. Wentzel, U. Morbiducci, and D. Gallo, “Divergence of the normalized wall shear stress as an effective computational template of low-density lipoprotein polarization at the arterial blood-vessel wall interface.,” Comput. Methods Programs Biomed. **226**, 107174 (2022).

[27] D. Küchemann, “Report on the I.U.T.A.M. symposium on concentrated vortex motions in fluids,” J. Fluid Mech. **21**(1), 1–20 (1965).

[28] G. Pedrizzetti, G. La Canna, O. Alfieri, and G. Tonti, “The vortex—an early predictor of cardiovascular outcome?,” Nat. Rev. Cardiol. **11**(9), 545–553 (2014).

[29] M. Gharib, E. Rambod, A. Kheradvar, D.J. Sahn, and J.O. Dabiri, “Optimal vortex formation as an index of cardiac health.,” Proc. Natl. Acad. Sci. U. S. A. **103**(16), 6305–6308 (2006).

[30] A. Amodeo, M. Grigioni, G. Oppido, C. Daniele, G. D’Avenio, G. Pedrizzetti, S. Giannico, S. Filippelli, and R.M. Di Donato, “The beneficial vortex and best spatial arrangement in total extracardiac cavopulmonary connection,” J. Thorac. Cardiovasc. Surg. **124**(3), 471–478 (2002).

[31] P. Dyverfeldt, C. Trenti, M. Ziegler, N. Bjarnegård, and M. Lindenberger, “Helical flow in tortuous aortas and its relationship to turbulence: A whole-aorta 4D flow MRI study.,” Front. Cardiovasc. Med. **10**, 1124604 (2023).

[32] U. Morbiducci, R. Ponzini, G. Rizzo, M. Cadioli, A. Esposito, F. De Cobelli, A. Del Maschio, F.M. Montevecchi, and A. Redaelli, “In vivo quantification of helical blood flow in human aorta by time-resolved three-dimensional cine phase contrast magnetic resonance imaging.,” Ann. Biomed. Eng. **37**(3), 516–531 (2009).

[33] N.C. Wild, K. V Bulusu, and M.W. Plesniak, “Vortical Structures Promote Atheroprotective Wall Shear Stress Distributions in a Carotid Artery Bifurcation Model,” Bioengineering **10**(9), (2023).

[34] D. Gallo, D.A. Steinman, P.B. Bijari, and U. Morbiducci, “Helical flow in carotid bifurcation as surrogate marker of exposure to disturbed shear.,” J. Biomech. **45**(14), 2398–2404 (2012).

[35] G. De Nisco, A.M. Kok, C. Chiastra, D. Gallo, A. Hoogendoorn, F. Migliavacca, J.J. Wentzel, and U. Morbiducci, “The Atheroprotective Nature of Helical Flow in Coronary Arteries.,” Ann. Biomed. Eng. **47**(2), 425–438 (2019).

[36] A. Kheradvar, and G. Pedrizzetti, *Vortex Formation in the Cardiovascular System* (Springer London, 2012).

[37] N. Tomizawa, S. Fujimoto, T. Mita, D. Takahashi, Y. Nozaki, R. Fan, A. Kudo, Y. Kawaguchi, K. Takamura, M. Hiki, M. Kurita, K.K. Kumamaru, H. Watada, T. Minamino, and S. Aoki, “Coronary Artery Vorticity to Predict Functional Plaque Progression in Participants with Type 2 Diabetes Mellitus,” Radiol. Cardiothorac. Imaging **5**(4), e230016 (2023).

[38] M. Chu, C. von Birgelen, Y. Li, J. Westra, J. Yang, N.R. Holm, J.H.C. Reiber, W. Wijns, and S. Tu, “Quantification of disturbed coronary flow by disturbed vorticity index and relation with fractional flow reserve,” Atherosclerosis **273**, 136–144 (2018).

[39] M. Lodi Rizzini, A. Candreva, V. Mazzi, M. Pagnoni, C. Chiastra, J.-P. Aben, S. Fournier, S. Cook, O. Muller, B. De Bruyne, T. Mizukami, C. Collet, D. Gallo, and U. Morbiducci, “Blood Flow Energy Identifies Coronary Lesions Culprit of Future Myocardial Infarction,” Ann. Biomed. Eng. **52**(2), 226–238 (2024).

[40] N. Varble, G. Trylesinski, J. Xiang, K. Snyder, and H. Meng, “Identification of vortex structures in a cohort of 204 intracranial aneurysms.,” J. R. Soc. Interface **14**(130), (2017).

[41] B.J. Chung, F. Mut, C.M. Putman, F. Hamzei-Sichani, W. Brinjikji, D. Kallmes, C.M. Jimenez, and J.R. Cebral, “Identification of Hostile Hemodynamics and Geometries of Cerebral Aneurysms: A Case-

Control Study.," AJNR. Am. J. Neuroradiol. **39**(10), 1860–1866 (2018).

[42] E.L. Leemans, B.M.W. Cornelissen, C.H. Slump, C.B.L.M. Majoie, J.R. Cebral, and H.A. Marquering, "Comparing Morphology and Hemodynamics of Stable-versus-Growing and Grown Intracranial Aneurysms.," AJNR. Am. J. Neuroradiol. **40**(12), 2102–2110 (2019).

[43] M. Dabagh, P. Nair, J. Gounley, D. Frakes, L.F. Gonzalez, and A. Randles, "Hemodynamic and morphological characteristics of a growing cerebral aneurysm.," Neurosurg. Focus **47**(1), E13 (2019).

[44] T. Ngwenya, D. Grundlingh, and M.N. Ngoepe, "Influence of vortical structures on fibrin clot formation in cerebral aneurysms: A two-dimensional computational study," J. Biomech., 111994 (2024).

[45] J. Biasetti, F. Hussain, and T.C. Gasser, "Blood flow and coherent vortices in the normal and aneurysmatic aortas: a fluid dynamical approach to intra-luminal thrombus formation," J. R. Soc. Interface **8**(63), 1449–1461 (2011).

[46] A. Arzani, and S.C. Shadden, "Characterization of the transport topology in patient-specific abdominal aortic aneurysm models.," Phys. Fluids (1994). **24**(8), 81901 (2012).

[47] Y. Qiu, J. Wang, J. Zhao, T. Wang, T. Zheng, and D. Yuan, "Association Between Blood Flow Pattern and Rupture Risk of Abdominal Aortic Aneurysm Based on Computational Fluid Dynamics.," Eur. J. Vasc. Endovasc. Surg. Off. J. Eur. Soc. Vasc. Surg. **64**(2–3), 155–164 (2022).

[48] B.R. Morton, "The generation and decay of vorticity," Geophys. Astrophys. Fluid Dyn. **28**(3–4), 277–308 (1984).

[49] M.S. Chong, J.P. Monty, C. Chin, and I. Marusic, "The topology of skin friction and surface vorticity fields in wall-bounded flows," J. Turbul. **13**(null), N6 (2012).

[50] R.C. Chin, J.P. Monty, M.S. Chong, and I. Marusic, "Conditionally averaged flow topology about a critical point pair in the skin friction field of pipe flows using direct numerical simulations," Phys. Rev. Fluids **3**(11), 114607 (2018).

[51] J.R. Cebral, F. Mut, J. Weir, and C.M. Putman, "Association of hemodynamic characteristics and cerebral aneurysm rupture.," AJNR. Am. J. Neuroradiol. **32**(2), 264–270 (2011).

[52] J.Z. Wu, and J.M. Wu, in edited by J.W. Hutchinson and T.Y.B.T.-A. in A.M. Wu (Elsevier, 1996), pp. 119–275.

[53] A.M. Gambaruto, and A.J. João, "Computers & Fluids Flow structures in cerebral aneurysms," Comput. Fluids **65**, 56–65 (2012).

[54] C. Garth, X. Tricoche, and G. Scheuermann, in *IEEE Vis. 2004* (2004), pp. 329–336.

[55] C. Chnafa, P. Bouillot, O. Brina, M. Najafi, B.M.A. Delattre, M.I. Vargas, V.M. Pereira, and D.A. Steinman, "Errors in power-law estimations of inflow rates for intracranial aneurysm CFD.," J. Biomech. **80**, 159–165 (2018).

[56] N.M. Cancelliere, M. Najafi, O. Brina, P. Bouillot, M.I. Vargas, K.-O. Lovblad, T. Krings, V.M. Pereira, and D.A. Steinman, "4D-CT angiography versus 3D-rotational angiography as the imaging modality for computational fluid dynamics of cerebral aneurysms," J. Neurointerv. Surg. **12**(6), 626 LP – 630 (2020).

[57] W.E. Higgins, and E.J. Ojard, "Interactive morphological watershed analysis for 3D medical

images," Comput. Med. Imaging Graph. **17**(4), 387–395 (1993).

[58] M. Mortensen, and K. Valen-Sendstad, "Oasis: A high-level/high-performance open source Navier–Stokes solver," Comput. Phys. Commun. **188**, (2015).

[59] Y. Wang, Y. Gao, J. Liu, and C. Liu, "Explicit formula for the Liutex vector and physical meaning of vorticity based on the Liutex-Shear decomposition," J. Hydrodyn. **31**(3), 464–474 (2019).

[60] C. Liu, Y. Gao, S. Tian, and X. Dong, "Rortex - A new vortex vector definition and vorticity tensor and vector decompositions," Phys. Fluids **30**(3), (2018).

[61] S. Tian, Y. Gao, X. Dong, C. Liu, and W. Jian, "A Definition of Vortex Vector and Vortex," Univ. Sci. Technol. Nanjing, Jiangsu, China **1**(1), 1–26 (2016).

[62] B. Pang, Y. Ding, and Y. Wang, "Flow behavior analysis in boundary layer transition based on the Liutex–shear decomposition," AIP Adv. **13**(2), (2023).

[63] P. Shrestha, C. Nottage, Y. Yu, O. Alvarez, and C. Liu, "Stretching and shearing contamination analysis for Liutex and other vortex identification methods," Adv. Aerodyn. **3**(1), 8 (2021).

[64] C. Roloff, and P. Berg, "Effect of flow diverter stent malposition on intracranial aneurysm hemodynamics-An experimental framework using stereoscopic particle image velocimetry.," PLoS One **17**(3), e0264688 (2022).

[65] C.M. Schirmer, and A.M. Malek, "Critical influence of framing coil orientation on intra-aneurysmal and neck region hemodynamics in a sidewall aneurysm model.," Neurosurgery **67**(6), 1692–702; discussion 1702 (2010).

[66] A.E. Perry, and B.D. Fairlie, in *Int. Union Theor. Appl. Mech. Int. Union Geod. Geophys.*, edited by F.N. Frenkiel and R.E.B.T.-A. in G. Munn (Elsevier, 1975), pp. 299–315.

## FIGURES

### Figure 1

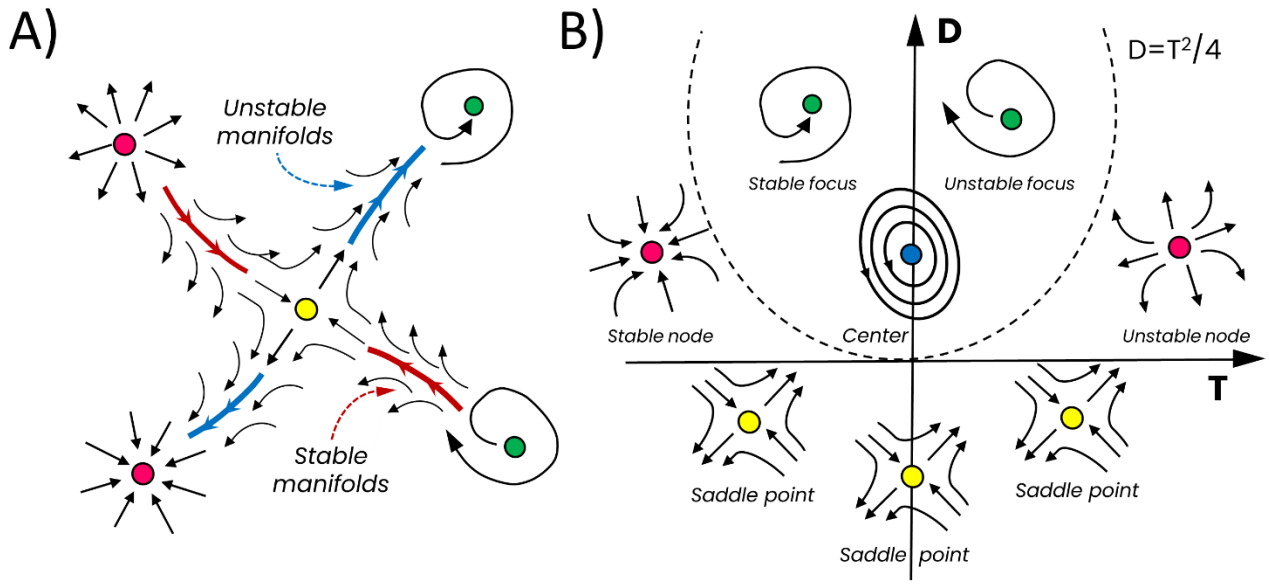


**Figure 1** A) Explanatory sketch of the theoretically possible stable/unstable manifold configurations connecting fixed points; B) theoretically possible configurations for a fixed point of a vector field in the T-D plane, where T and D refer to the trace and determinant of the Jacobian matrix of the vector field respectively. The dotted line represents the *critical quadratic curve* splitting the D>0 region in two subregions where the eigenvalues of the Jacobian matrix of the vector field are complex or real numbers. Inspired by Perry and Fairlie (1975) [66].

### Figure 2

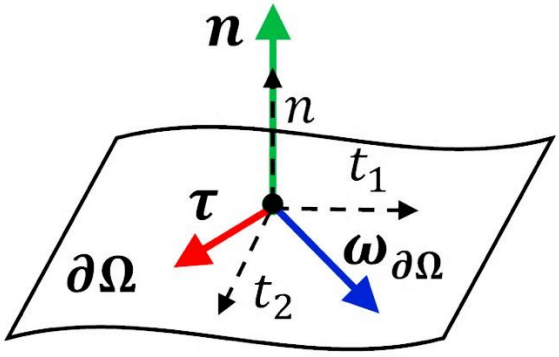


**Figure 2** Sketch of WSS (red arrow) and SV (blue arrow) vectors forming an orthogonal pair ($\boldsymbol{\tau}$, $\boldsymbol{\omega}_{\partial\Omega}$) on a stationary curved wall $\partial\Omega$ and the local coordinate system $(t_1, t_2, n)$ such that the $t_1 - t_2$ plane identifies the local tangent plane to $\partial\Omega$.

**Figure 3**

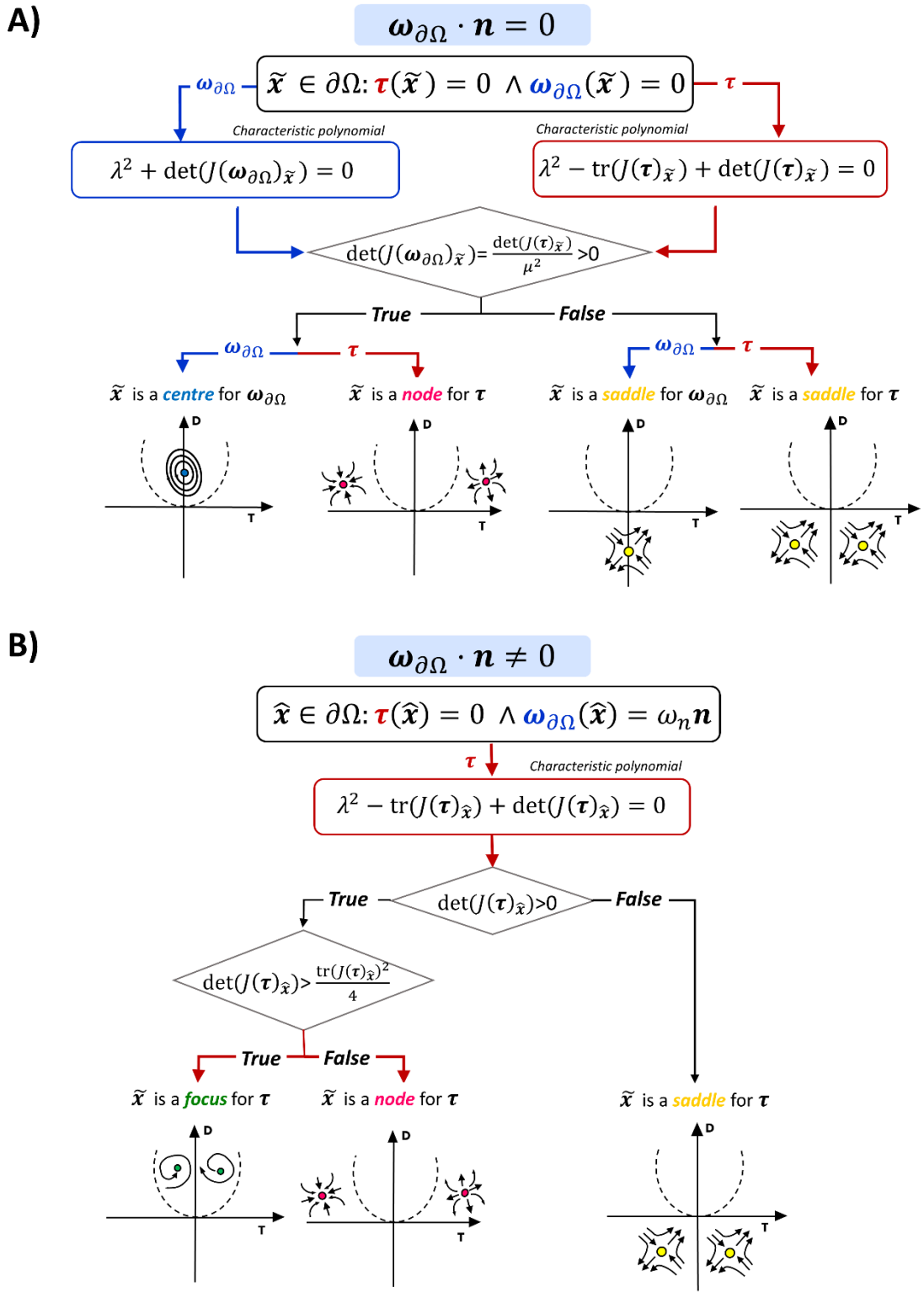


**Figure 3** A) Chart of the stability analysis of WSS and SV fixed points when the SV is purely tangent to the luminal surface; B) Chart of the stability analysis of WSS fixed points when the SV is not a fixed point.

## Figure 4

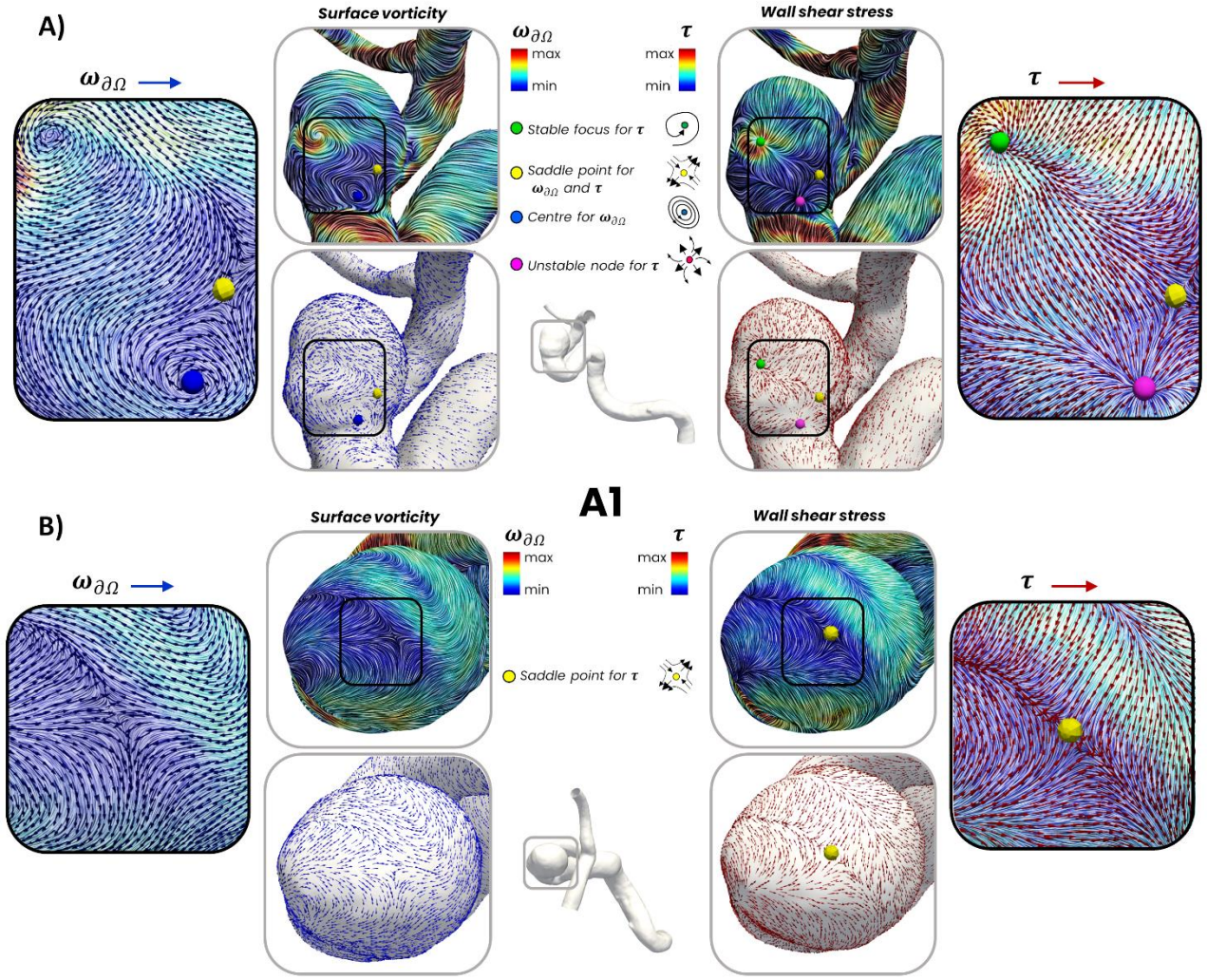


**Figure 4** Visualization of instantaneous SV (left panel) and WSS (right panel) field lines and vector fields on the luminal surface of intracranial aneurysm model A1. Flow visualizations refer to mid acceleration phase in systole. SV and WSS fixed points are depicted. Two different views are displayed: A) front view and B) top view. Four insets zooming on fixed points locations are displayed to appreciate the field topology in their neighborhood.

## Figure 5

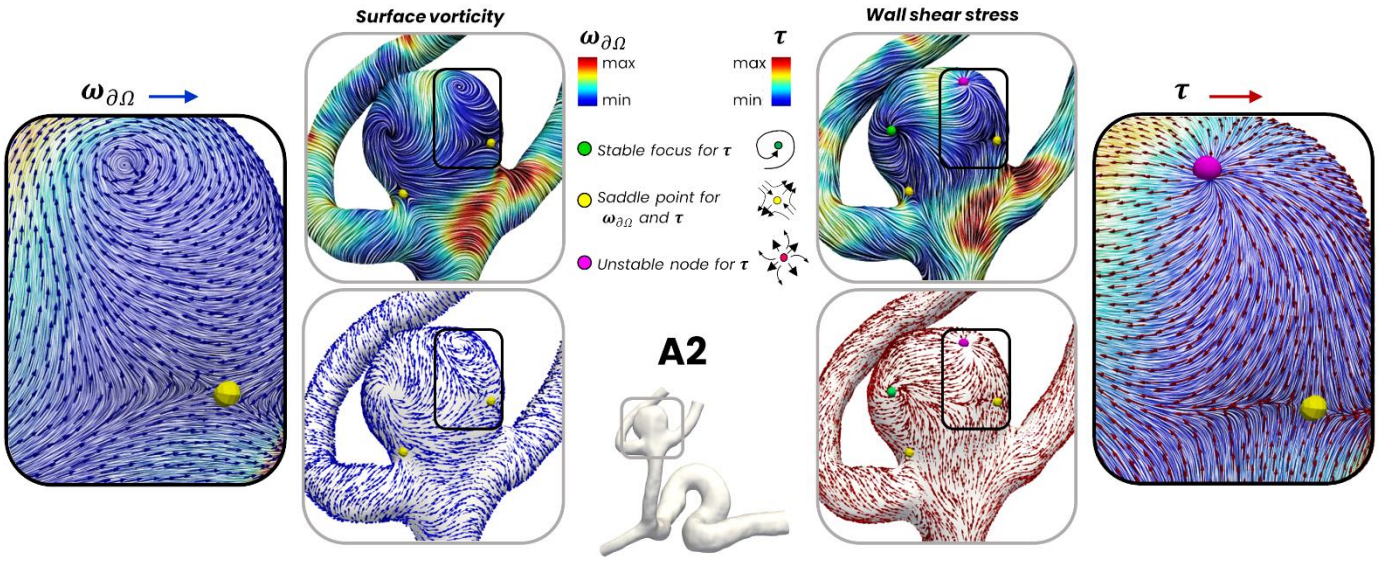


**Figure 5** Visualization of Instantaneous SV (left panel) and WSS (right panel) field lines and vector fields on the luminal surface of intracranial aneurysm model A2. Flow visualizations refer to mid acceleration phase in systole. SV and WSS fixed points are depicted. Two insets zooming on fixed points locations are displayed to appreciate the field topology in their neighborhood.

## Figure 6

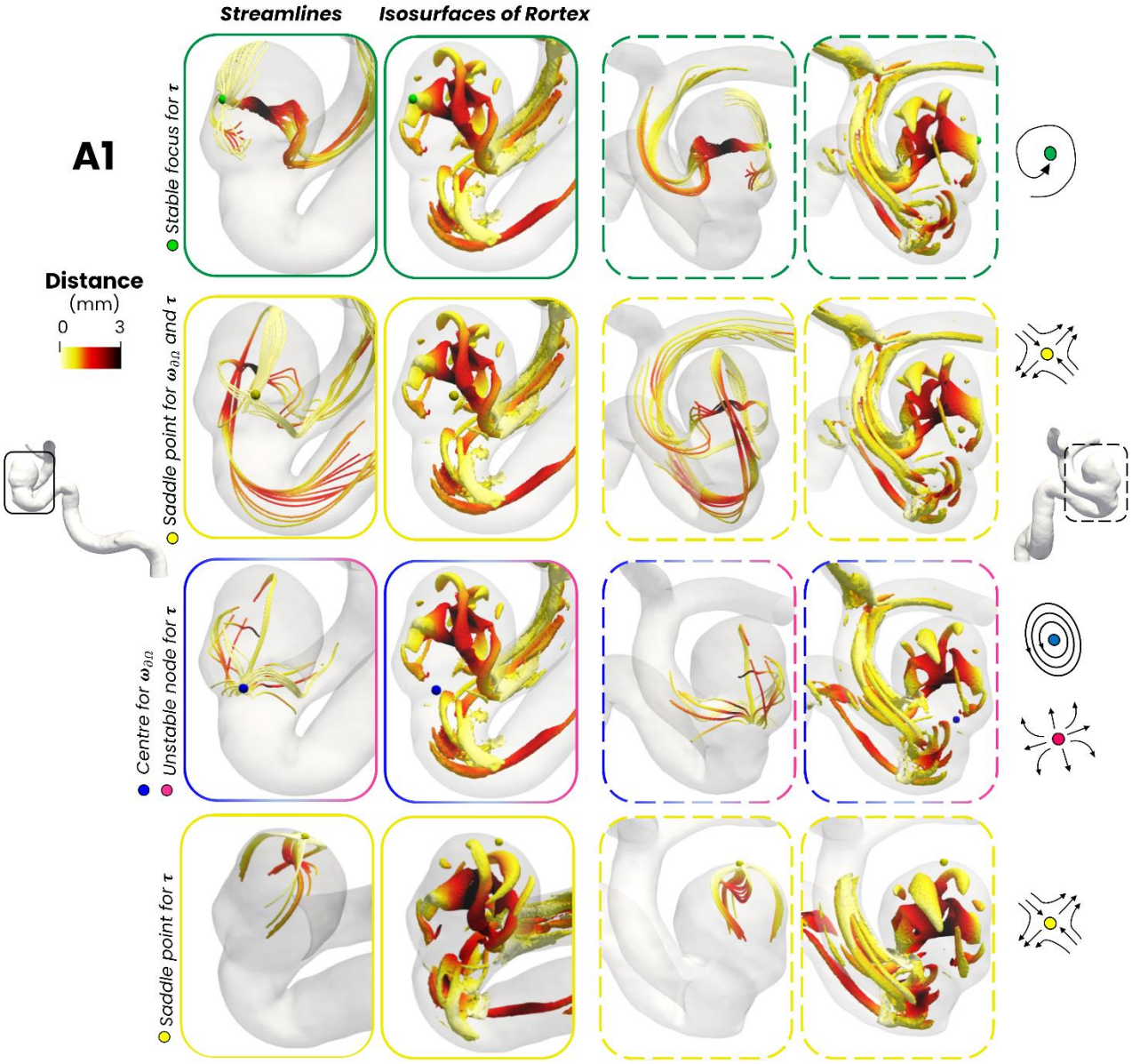


**Figure 6** Instantaneous velocity streamlines and $\boldsymbol{R}$ (the rotational part of vorticity) magnitude isosurfaces inside the intracranial aneurysm model A1. Flow visualizations refer to mid acceleration phase in systole. Both streamlines and $\boldsymbol{R}$ isosurfaces are coloured with the distance from the surface to highlight their contact with the wall. Four insets are displayed to appreciate the intravascular fluid structures interacting with the wall to shape the WSS topological skeleton. Two different views are displayed: one indicated by solid frames (left) and a complementary view indicated by dashed frames (right).

**Figure 7**

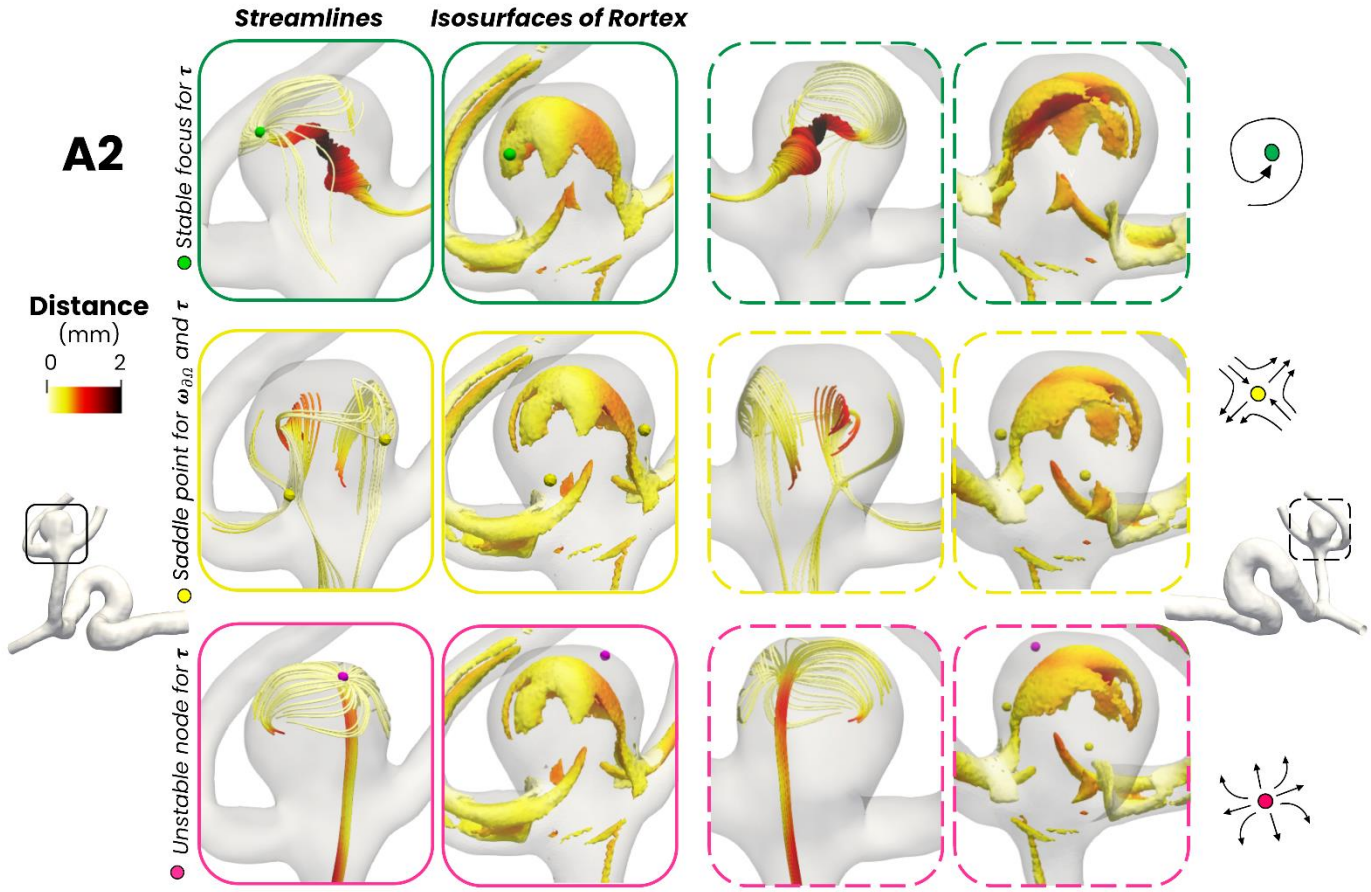


**Figure 7** Instantaneous velocity streamlines and $\boldsymbol{R}$ (the rotational part of vorticity) magnitude isosurfaces inside the intracranial aneurysm model A2. Flow visualizations refer to mid acceleration phase in systole. Both streamlines and $\boldsymbol{R}$ isosurfaces are coloured with the distance from the surface to highlight their contact with the wall. Three insets are displayed to appreciate the intravascular fluid structures interacting with the wall to shape the WSS topological skeleton. Two different views are displayed: one indicated by solid frames (left) and a complementary view indicated by dashed frames (right).

## Figure 8

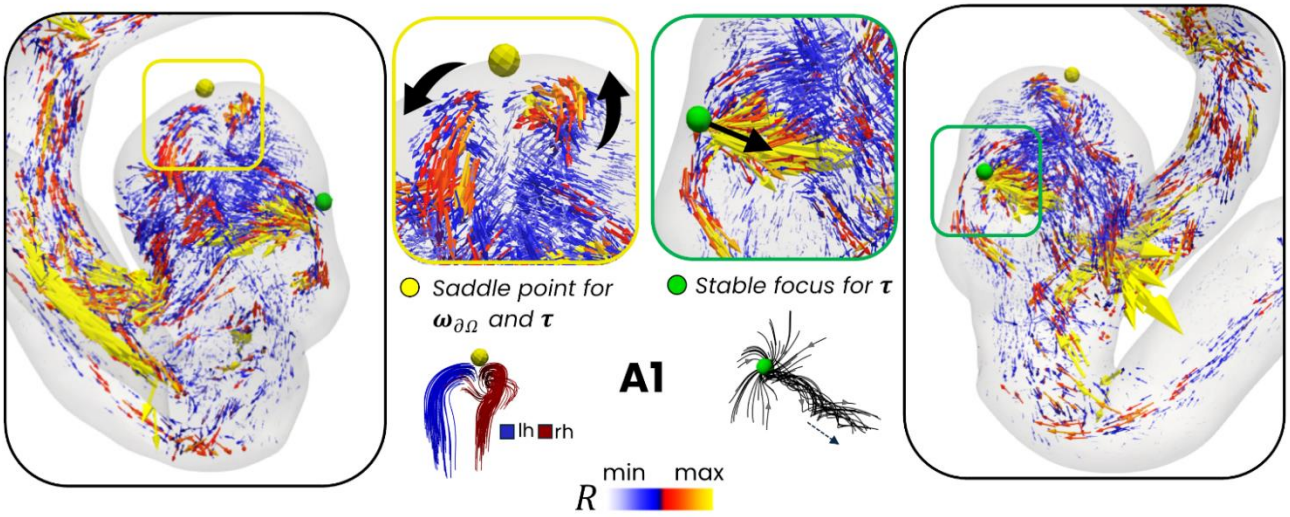


**Figure 8** Visualization of the $\boldsymbol{R}$ vector field (the rotational part of vorticity) colored with the $\boldsymbol{R}$ magnitude inside the intracranial aneurysm model A1. Flow visualizations refer to mid acceleration phase in systole. Two insets are displayed to appreciate $\boldsymbol{R}$ vectors direction, highlighting the presence of: (i) two counter-rotating vortex structures in correspondence with WSS and SV saddle points; (ii) a highly rotational fluid structure emanating from the wall where the WSS stable focus is located. lh: left-handed; rh: right-handed.

**Figure 9**

| ***WSS* fixed point** | ***SV* fixed point** | ***Near-wall flow structures*** |
|---|---|---|
| ***WSS*** has a fixed point when ***SV*** has a fixed point | | |
| Stable node | Centre | Null vorticity flux normal to the wall |
| Unstable node | Centre | Null vorticity flux normal to the wall |
| Saddle | Saddle | Null vorticity flux normal to the wall |
| ***WSS*** has a fixed point, but ***SV*** does not | | |
| Stable node | No SV fixed point | Non-rotational fluid structure emanating from the wall |
| Unstable node | No SV fixed point | Non-rotational fluid structure impinging to the wall |
| Stable focus | No SV fixed point | Rotational fluid structure emanating from the wall |
| Unstable focus | No SV fixed point | Rotational fluid structure impinging to the wall |
| Saddle | No SV fixed point | Two counter-rotating fluid structures |

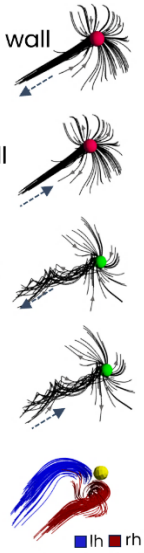


**Figure 9** Summary of the nature of the theoretically admitted relationships between WSS fixed points, SV fixed points and near-wall flow fluid structures when the SV (i) is purely tangent to the luminal surface, and (ii) when it is not. lh: left-handed; rh: right-handed.